

ARTICLE OPEN

Efficient Ohmic contacts and built-in atomic sublayer protection in MoSi₂N₄ and WSi₂N₄ monolayersQianqian Wang^{1,2}, Liemao Cao^{3✉}, Shi-Jun Liang⁴, Weikang Wu^{2,5}, Guangzhao Wang^{6,1,2}, Ching Hua Lee⁶, Wee Liat Ong^{7,8}, Hui Ying Yang⁹, Lay Kee Ang^{1✉}, Shengyuan A. Yang^{1,2✉} and Yee Sin Ang^{1✉}

Metal contacts to two-dimensional (2D) semiconductors are often plagued by the strong Fermi level pinning (FLP) effect which reduces the tunability of the Schottky barrier height (SBH) and degrades the performance of 2D semiconductor devices. Here, we show that MoSi₂N₄ and WSi₂N₄ monolayers—an emerging 2D semiconductor family with exceptional physical properties—exhibit strongly suppressed FLP and wide-range tunable SBH. An exceptionally large SBH slope parameter of $S \approx 0.7$ is obtained which outperforms the vast majority of other 2D semiconductors. Such intriguing behavior arises from the septuple-layered morphology of MoSi₂N₄ and WSi₂N₄ monolayers in which the semiconducting electronic states are protected by the outlying Si–N sublayer. We identify Ti, Sc, and Ni as highly efficient Ohmic contacts to MoSi₂N₄ and WSi₂N₄ with zero interface tunneling barrier. Our findings reveal the potential of MoSi₂N₄ and WSi₂N₄ as a practical platform for designing high-performance and energy-efficient 2D semiconductor electronic devices.

npj 2D Materials and Applications (2021)5:71; <https://doi.org/10.1038/s41699-021-00251-y>

INTRODUCTION

Electrical contacts between metals and semiconductors are ubiquitous in modern electronic and optoelectronic devices. An interfacial potential barrier, known as the Schottky barrier (SB), is commonly formed at the metal/semiconductor interface. In electronics and optoelectronics applications, the presence of a sizable Schottky barrier height (SBH), typically larger than a few $k_B T$, can severely impede the charge injection efficiency¹. As the SBH is intimately linked to the contact resistance at the metal/semiconductor contact^{2,3}, reducing the SBH at the metal/semiconductor contact has become one of the key challenges towards energy-efficient and high-speed semiconductor devices.

In a metal/semiconductor contact, SBH arises from the mismatch between the metal work function (W_M) and the semiconductor electron affinity E_{ea} (n-type Schottky contact) or ionization potential E_{ip} (p-type Schottky contact). The SBH across a metal/semiconductor contact can be phenomenologically captured by the modified Schottky–Mott (SM) rule^{4–7},

$$\Phi_{Be} = S_e(W_M - E_{ea}) + c_e \quad (1)$$

$$\Phi_{Bh} = S_h(E_{ip} - W_M) + c_h, \quad (2)$$

where the subscript “e” and “h” denote n- and p-type contacts, respectively, $c_{e(h)}$ is a material- and contact-dependent term⁷, and Φ_{Be} and Φ_{Bh} is the electron-type and hole-type SBH, respectively. Here, the slope parameter, $S_{e(h)}$, is defined as

$$S_{e(h)} \equiv \left| \frac{d\Phi_{Be(h)}}{dW_M} \right| \quad (3)$$

which is an important phenomenological parameter widely used in characterizing the deviation of the SBH from the ideal SM limit ($S = 1$). In realistic metal/semiconductor contacts, $S \ll 1$ due to the presence of multiple nonideal factors, such as the formation of metal-induced gap states, defect-induced gap states, mid-gap states, and interface dipole, as well as the modifications of the electronic band structures of the semiconductor when contacted by metals^{6,7}. In this case, the SBH is pinned to a narrow range of value—an adverse effect commonly known as the Fermi level pinning (FLP).

In the few-atom-thick limit, two-dimensional (2D) semiconductors⁸, such as MoS₂ and WS₂⁹, continue to be plagued by FLP¹⁰. Although 2D semiconductors and their van der Waals (VDW) heterostructures has shown great promises in low-power electronics¹¹, optoelectronics¹², and neuromorphic applications¹³, the lack of wide-range tunable SBH—commonplace in most 2D semiconductors—has severely impeded the development of high-performance nanodevices. Particularly, the metalization of a 2D semiconductor by the contacting metal often substantially alters the electronic structures of the heterostructure via the generation of mid-gap states^{14,15}, causing strong FLP effect that leads to a poor SBH tunability¹⁵. For the vast majority of 2D semiconductors, S is typically less than 0.4 as predicted by density functional theory (DFT) calculations, and are even lower in experimental measurements due to the inevitable presence of defects at the contact interface. To resurrect a wide-range tunable SBH in 2D semiconductors, atomically sharp VDW metal/2D-semiconductor electrical contacts have been proposed¹⁶. Such VDW-type contacts harness the weak VDW interfacial coupling to reduce the metal/semiconductor interactions, yielding an $S \approx 1$ that approaches

¹Science, Mathematics and Technology, Singapore University of Technology and Design, Singapore, Singapore. ²Research Laboratory of Quantum Materials, Singapore University of Technology and Design, Singapore, Singapore. ³College of Physics and Electronic Engineering, Hengyang Normal University, Hengyang, China. ⁴National Laboratory of Solid State Microstructures, School of Physics, Collaborative Innovation Center of Advanced Microstructures, Nanjing University, Nanjing, China. ⁵Division of Physics and Applied Physics, School of Physical and Mathematical Sciences, Nanyang Technological University, Singapore, Singapore. ⁶Department of Physics, National University of Singapore, Singapore, Singapore. ⁷Zhejiang University–University of Illinois at Urbana-Champaign Institute (ZJU–UIUC) College of Energy Engineering, Zhejiang University, Hangzhou, Zhejiang, China. ⁸State Key Laboratory of Clean Energy Utilization, Zhejiang University, Hangzhou, Zhejiang, China. ⁹Engineering Product Development, Singapore University of Technology and Design, Singapore, Singapore. ✉email: liemao_cao@hynu.edu.cn; ricky_ang@sutd.edu.sg; shengyuan_yang@sutd.edu.sg; yeesin_ang@sutd.edu.sg

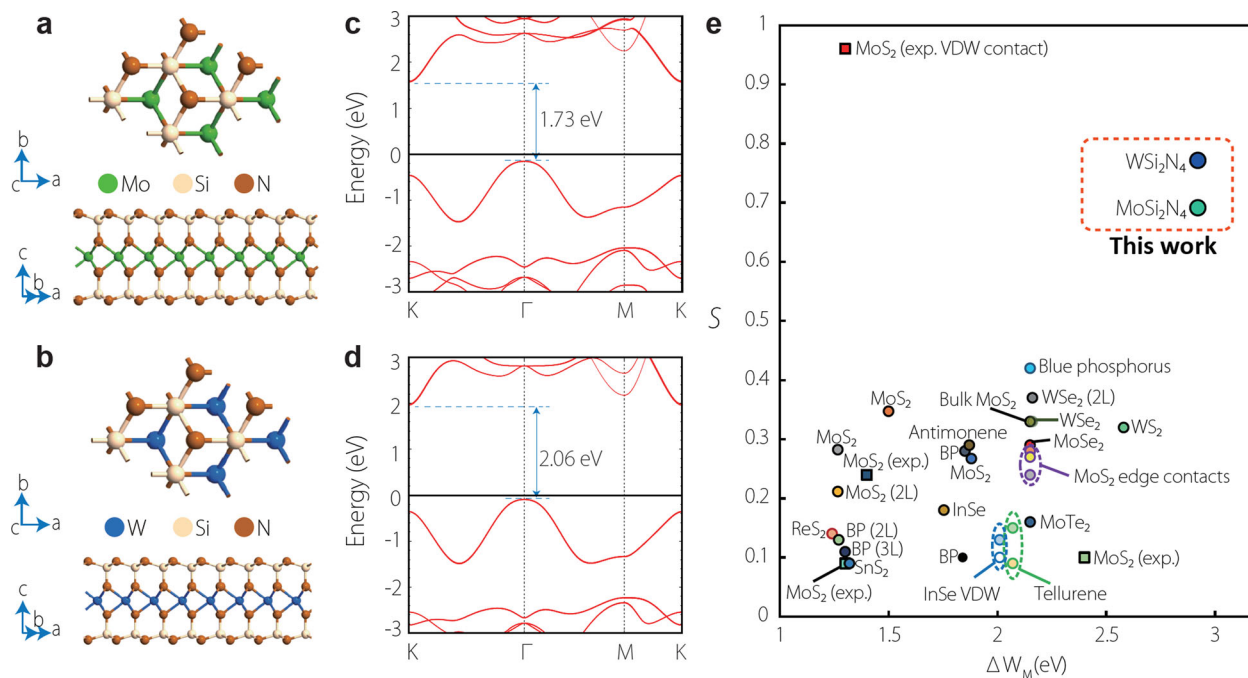


Fig. 1 Lattice structures, energy band structures, and S parameters of MoSi_2N_4 and WSi_2N_4 monolayers. **a** Top and side view of MoSi_2N_4 monolayer, **b** same as **a** for WSi_2N_4 monolayer, **c** and **d** electronic band structures of isolated MoSi_2N_4 and WSi_2N_4 monolayer, respectively. **e** The slope parameter S versus the metal work function range (ΔW_M) of a large variety of 2D semiconductors, showing exceptionally large S for MoSi_2N_4 and WSi_2N_4 . Included are the DFT simulations of MoS_2 [face contact^{14,15,27,41} and edge contact²⁷], WS_2 ^{27,39}, WSe_2 ⁴⁰, MoSe_2 ²⁷, MoTe_2 ²⁷, black phosphorus^{42–45}, blue phosphorus⁴⁵, antimonene⁴⁶, tellurene⁴⁷, InSe [3D metal contact³⁶ and 2D metal VDW contact³⁷], ReS_2 ³⁸, and the experimental results of MoS_2 ^{48,49} and SnS_2 ⁵⁰. The notations “2L” and “3L” denote bilayer and trilayer, respectively. The MoSi_2N_4 and WSi_2N_4 are highlighted by the dashed box.

the ideal SM limit^{17–19}. However, as VDW-type contact often involves complex fabrication techniques, a 2D semiconductor class that can inherently achieve substantial Fermi level unpinning without necessarily relying on the VDW contact paradigm remains elusive thus far.

In this work, we perform a first-principle DFT investigation to study the metal contact properties in the recently discovered synthetic 2D monolayers, MoSi_2N_4 and WSi_2N_4 ^{20,21}. We focus on face-type contact¹ as it is widely employed in both the experimental design of 2D nanodevices^{18,19,22–26} and the computational contact simulation studies^{15,17,27–29}. The recent demonstrations of ultralow contact resistance and the high on-state current in face-contacted 2D semiconductor^{18,19,22} also reveal the technological importance of face-type contact towards the development of high-performance 2D nanodevices³⁰. We show that, in contrary to the common knowledge that 2D semiconductors are prone to strong FLP, MoSi_2N_4 , and WSi_2N_4 monolayers exhibit strongly suppressed FLP and excellent SBH tunability without relying on the VDW-type contact engineering. The SBH is widely tunable in MoSi_2N_4 and WSi_2N_4 monolayers, reaching an exceptionally high slope parameter of $S = 0.69$ and $S = 0.77$, respectively—a value much larger than other commonly studied 2D semiconductors. The FLP suppression originates from the unusual morphology and the electronic properties of MoSi_2N_4 and WSi_2N_4 monolayers, in which the semiconducting states residing in Mo–N or W–N inner core-layer are protected by the outlying Si–N atomic layers—an intriguing mechanism not found in other classes of 2D semiconductors. Our results reveal MoSi_2N_4 and WSi_2N_4 monolayer as an unusual 2D semiconductor class with built-in atomic layer protection, thus opening up an alternative and complementary route to the VDW contact paradigm towards efficient SBH tuning and high-performance electrical contact engineering.

RESULTS

Electronic properties of MoSi_2N_4 and WSi_2N_4 metal contacts

The 2D monolayers of MoSi_2N_4 and WSi_2N_4 blue [see Fig. 1a, b for the lattice structures of MoSi_2N_4 and WSi_2N_4] belong to the family of MA_2Z_4 synthetic 2D layered materials with no known 3D parent materials (M = early transition metal, A = Si or Ge, Z = N, P, or As). The MA_2Z_4 2D material family covers a wide variety of semiconducting, metallic, insulating, and magnetic phases, offering an exciting platform for the exploration of 2D semiconductor physics and device applications^{31–35}. Structurally, MoSi_2N_4 (WSi_2N_4) monolayer is composed of a Mo–N (W–N) monolayer sandwiched by two Si–N layers. Electronically, MoSi_2N_4 and WSi_2N_4 monolayers are indirect band gap semiconductors with band gap values of 1.73 and 2.06 eV, respectively [Fig. 1c, d], and exhibit excellent structural stability and mechanical strength²⁰.

We perform first-principles DFT simulations to model the heterostructure composed of MoSi_2N_4 and WSi_2N_4 monolayers contacted by a large variety of metals (3D metals Sc, In, Ti, Ag, Cu, Ni, Au, Pd, Pt; 2D semimetal graphene; and 2D metal NbS_2 monolayer) with work function values ranging from 3.3 to 6.0 eV (see Method section for the DFT simulation procedures). Comparing with a large variety of previously reported 2D semiconductors^{14,15,27,36–51} [Fig. 1e], our calculation reveals an exceptionally large S -parameter for MoSi_2N_4 and WSi_2N_4 of $S = 0.69$ and $S = 0.77$, respectively, which spans over a large contacting metal work function range of $\Delta W_M = 2.7$ eV.

In general, the metal contacts to MoSi_2N_4 and WSi_2N_4 cover a large variety of contact types, including n-type Schottky contact, p-type Schottky contact, and Ohmic contact with zero SBH. The interlayer distance between the metal and 2D monolayers is less than 3 Å for Cu, Pd, Ti, and Ni (see Supplementary Tables 1 and 2), suggesting the prevalence of non-VDW-type metal contacts. In the following, we shall take Au and Ti metal contacts as illustrative examples of Schottky (Fig. 2) and Ohmic contacts (Fig. 3),

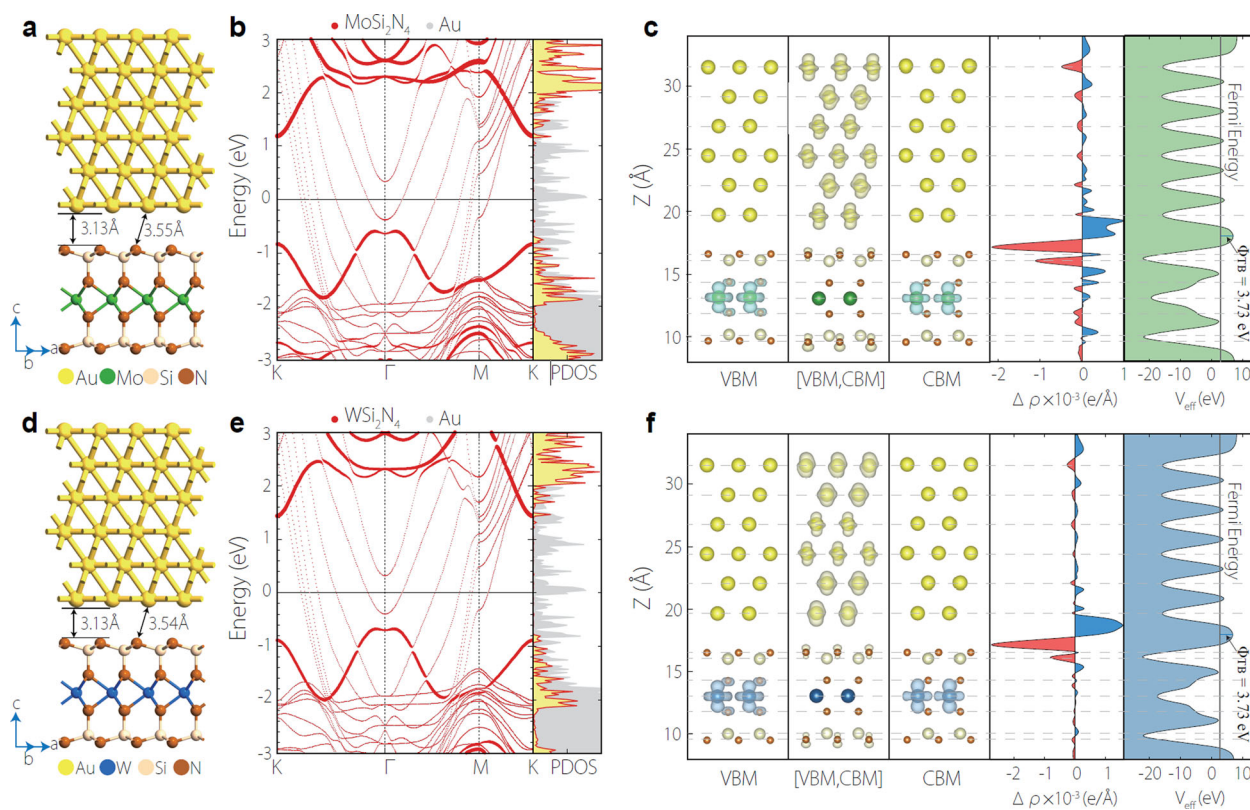


Fig. 2 Schottky contacts of Au/MoSi₂N₄ and Au/WSi₂N₄ - Structural and electronic properties. **a** The contact is composed of six layers of Au atoms contacting the MoSi₂N₄ monolayer. The interlayer distance is 3.13 Å and the minimum distance between Au and N atoms is 3.55 Å. **b** The projected electronic band structure and the partial density of states of Au/MoSi₂N₄ contact. The panels in **c** from left to right, show the spatial charge density distribution of VBM states, mid-gap states between VBM and CBM, and the CBM states, the differential charge density, and the electrostatic potential profile across the heterostructures. **d–f** Same as **a**, **b**, and **c**, respectively, for Au/WSi₂N₄ contact. The interlayer distance is 3.13 Å and the minimum distance between Au and N atoms is 3.54 Å.

respectively (see Supplementary Fig. 1 for the relaxed lattice structures of all metal contacts calculated in this work). The lattice structures of the Au and Ti contacts to MoSi₂N₄ and WSi₂N₄ monolayers are shown in Figs. 2a and 3a, respectively.

A closer inspection of the electronic band structures of the metal/MoSi₂N₄ and metal/WSi₂N₄ reveals intriguing behaviors. The metal/semiconductor heterostructures are nearly free of mid-gap states for all metals as revealed in the projected band structures and the partial density of states (PDOS) [Fig. 2b, e for Au Schottky contacts and Fig. 3b, e for Ti Ohmic contact, see also Supplementary Fig. 2 for the projected band structures and PDOS of other metal contacts]. By projecting the 2D semiconductor electronic states onto the band structures, we find that the semiconducting bands, particularly the electronic states around the valence band maximum (VBM) and the conduction band minimum (CBM), remain intact in all metal contacts, suggesting the near absence of mid-gap states within the semiconductor band gap. For Ti contact, despite being a close contact type with an exceedingly small interlayer distance of 1.75 and 1.78 Å, mid-gap states remain nearly absent [see PDOS in Fig. 3b, e], which is in stark contrast to metal-contacted MoS₂ where a large abundance of mid-gap states localizing in the Mo sites are created^{15,52}.

We further calculate the spatial charge density distribution around the VBM and the CBM, as well as the states between the VBM and the CBM. Intriguingly, the semiconducting electronic states are embedded deeply within inner Mo–N [Figs. 2c and 3c] and W–N core layer [Figs. 2f and 3f], while the mid-gap states between the VBM and CBM are mostly located in the metals and sparsely distributed in the outlying Si–N layers. Such metal-induced

mid-gap states decay rapidly without penetrating into the semiconducting inner core layer, thus leading to a much-weakened FLP. We also calculate the differential charge density ($\Delta\rho$) which reveals a significant charge redistribution across the metal/semiconductor contact interface [Figs. 2c, f and 3c, f]. As $\Delta\rho$ across the contact interface is asymmetrical, the formation of interface dipole is expected to modify the S parameter from the ideal SM limit (see Supplementary Fig. 4 for the calculated $\Delta\rho$ of other metal contacts).

The effective electrostatic potential profile, V_{eff} , across the metal/semiconductor contact is shown in the left-most panels of Fig. 2c, f for Au contact, and Fig. 3c, f for Ti contact. For contacts with V_{eff} higher than the Fermi level at the metal/semiconductor interface, the V_{eff} forms an interfacial tunneling potential barrier (denoted as Φ_{TB} in Figs. 2 and 3), which significantly impedes the charge injection efficiency. In the case of Au contact, the presence of a sizable barrier of $\Phi_{\text{TB}} \approx 3.13$ eV [Fig. 2c, f] reveals a much-reduced electron transmission across the metal/semiconductor contact. In contrast, the absence of Φ_{TB} in the case of Ti contact [Fig. 3c, f] reveals the potential of Ti as an efficient electrode to MoSi₂N₄ and WSi₂N₄ with a large electron transmission probability. The Φ_{TB} and the corresponding electron transmission probability of various metal contacts to MoSi₂N₄ and WSi₂N₄ will be discussed in detail below.

The absence of mid-gap states in the inner core layer and the finite charge transfer at the outlying Si–N layers reveals that the metal/semiconductor interaction affects mostly the outlying Si–N layers, predominantly via charge redistribution, without penetrating semiconducting Mo–N and W–N inner cores. Here the Si–N layer serves as an encapsulating layer and plays a vital role in

CMOS-compatible Ti Ohmic contact

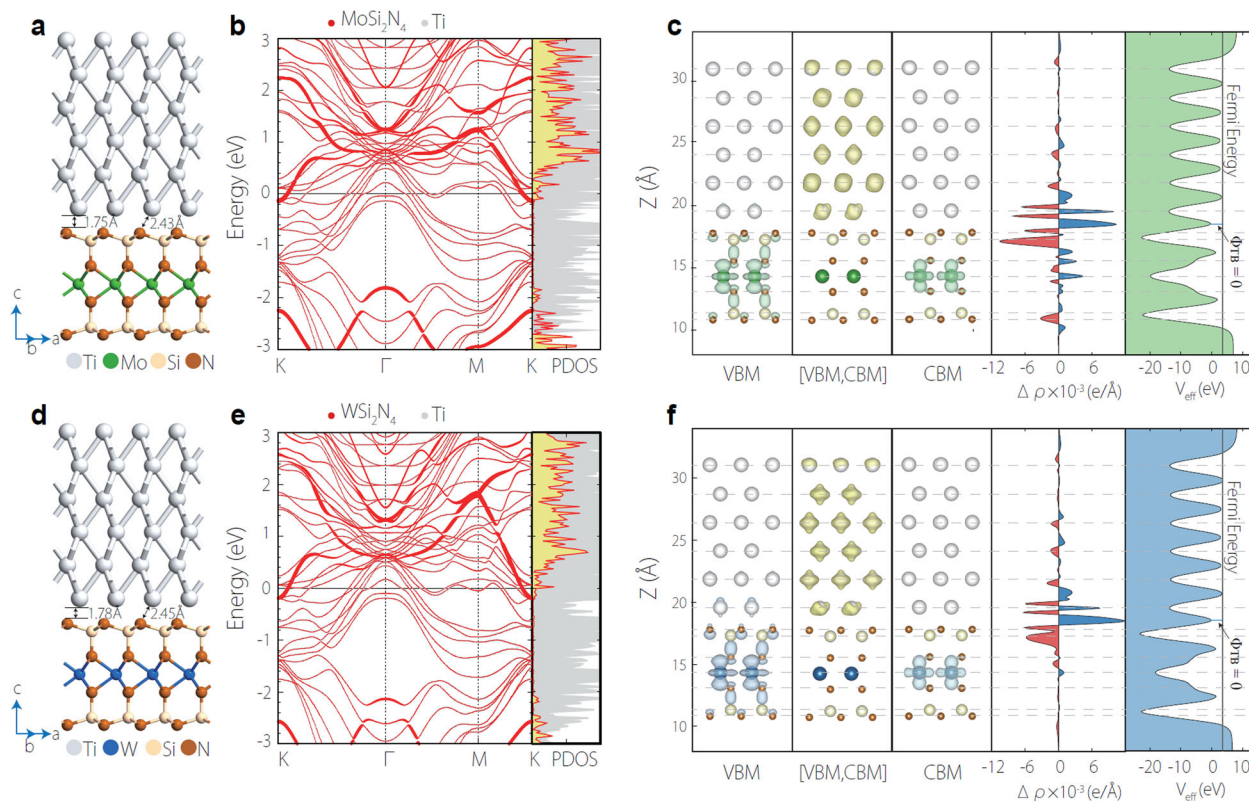


Fig. 3 Ohmic contacts of Ti/MoSi₂N₄ and Ti/WSi₂N₄—structural and electronic properties. **a** The contact is composed of six layers of Ti atoms contacting the MoSi₂N₄ monolayer. The interlayer distance is 1.75 Å and the minimum distance between Ti and N atoms is 2.43 Å. **b** The projected electronic band structure and the partial density of states of Ti/MoSi₂N₄ contact. The panels in **c** from left to right, show the spatial charge density distribution of VBM states, mid-gap states between VBM and CBM, and the CBM states, the differential charge density, and the electrostatic potential profile across the heterostructures. **d–f** Same as **a**, **b**, and **c**, respectively, for Ti/WSi₂N₄ contact. The interlayer distance is 1.78 Å and the minimum distance between Ti and N atoms is 2.45 Å.

preserving the semiconducting characteristics of MoSi₂N₄ and WSi₂N₄ monolayers. To verify the protective effect of Si–N layers⁵³, we simulate a close contact type of Au/MoSi₂N₄ and Au/WSi₂N₄ heterostructures by forcing the interlayer distance to 1.5 Å, compared to the fully relaxed value of about 3.13 Å (see Supplementary Fig. 3). The semiconducting band structures are well-preserved at this close-contact limit, thus confirming the robustness of the semiconducting states residing in the MoSi₂N₄ and WSi₂N₄ monolayers and the resilience against mid-gap states formation. Such unusual behavior, enabled by the septuple-layered morphology of MoSi₂N₄ and WSi₂N₄ monolayer, is not found in other commonly studied 2D semiconductors, such as transition metal dichalcogenides (TMDCs) and black phosphorus, in which an external insertion layer is often required to unpin the Fermi level^{54–56}. We further perform a comparison with monolayer MoS₂ by calculating the charge density distribution³⁹ and the electronic band structures of Sc/MoSi₂N₄ and the Sc/MoS₂ contacts in Fig. 4. The charge density plots in Fig. 4a, c shows the presence of a large amount of electrons from Sc atoms overlapping strongly with the MoS₂ layer [Fig. 4c] while the MoSi₂N₄ layer remains well-isolated from the electrons of Sc atoms [Fig. 4a]. Such electron overlap in Sc/MoS₂ directly leads to strong metal-semiconductor hybridization as evident from the band structure and the PDOS plot in Fig. 4d, which is in strong contrast to the case of Sc/MoSi₂N₄ in Fig. 4b where the electronic states around CBM and VBM remain intact.

As the CBM and VBM electronic states contribute dominantly to the carrier transport, the suppression of FLP due to the atomic-layer protection as discussed above can also be understood as the

consequence of having a transport channel that is spatially well-separated from the influence of the contacting metal atoms. In the case of MoS₂—a triple-layered structure which is morphologically much thinner than the septuple-layered MoSi₂N₄, the transport channel residing around the Mo atoms is in closer proximity with the contacting metal and hence the presence of stronger hybridization leads to a more severe FLP effect.

Interfacial tunneling potential barrier and Schottky barrier

As discussed above, the formation of a tunneling potential barrier, Φ_{TB} , at the metal/semiconductor gap impedes the charge injection efficiency⁵². The Φ_{TB} and the barrier width, d_{TB} can be determined from the effective electrostatic potential across the metal/semiconductor interface (see Supplementary Fig. 5). For both MoSi₂N₄ and WSi₂N₄ monolayers, Φ_{TB} ranges between 2.8 and over 5.1 eV, and the thickness d_{TB} ranges between 1.1 and 2 Å (see Supplementary Tables 1 and 2). The corresponding electron tunneling probability across the interface can be then calculated as,

$$\mathcal{T}(\Phi_{TB}, d_{TB}) = \exp\left(-\frac{4\pi\sqrt{2m_e\Phi_{TB}}d_{TB}}{\hbar}\right), \quad (4)$$

where m_e is the free electron mass. The $\mathcal{T}(\Phi_{TB}, d_{TB})$ calculated via Eq. (4) for various metal contacts are shown in Fig. 5a. For Sc, Ti, and Ni, the tunneling probability reaches 100% as $\Phi_{TB} = 0$. Particularly for Sc and Ti, both Φ_{TB} and Φ_B are zero in both MoSi₂N₄ and WSi₂N₄ monolayers—an indication of good Ohmic contacts with high charge injection efficiency. In contrast, the

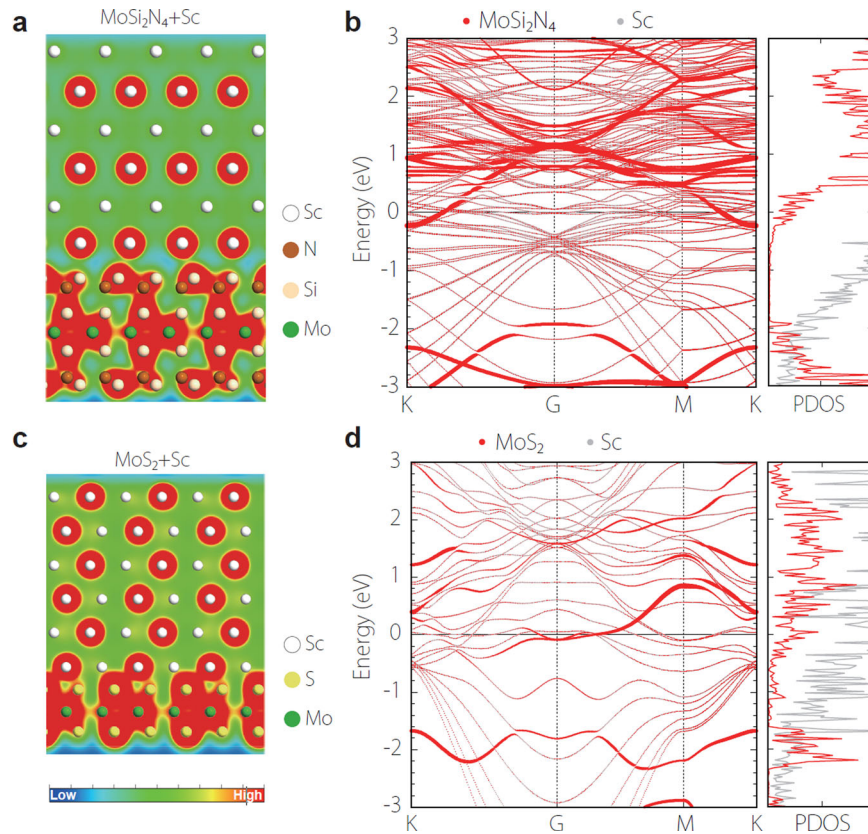


Fig. 4 Comparing Sc contacts to MoSi₂N₄ MoS₂. **a** Contour plots of total electron distribution of Sc/MoSi₂N₄. **b** Band structure and projected density of states of Sc/MoSi₂N₄. **c, d** Same as **b** and **c**, respectively, but for Sc/MoS₂.

VDW-type contacts, such as graphene and NbS₂ with interlayer distances greater than 3 Å, exhibit very low \mathcal{T} of less than 2%, which suggests a low electron transparency in such VDW-type interfaces.

Apart from tunneling probability, the extracted d_{TB} and Φ_{TB} can also be used to estimate the tunneling-specific resistivity (ρ_t)²². Based on Simmons tunneling injection model⁵⁷, ρ_t can be obtained as,

$$\rho_t \approx \frac{4\pi^2 \hbar d_{\text{TB}}^2}{e^2} \frac{\exp\left[\frac{2(2m_e)^{1/2}}{\hbar} a d_{\text{TB}} \Phi_{\text{TB}}^{1/2}\right]}{\frac{(2m_e)^{1/2}}{\hbar} a d_{\text{TB}} \Phi_{\text{TB}}^{1/2} - 1} \quad (5)$$

where $a = 1$ under the square-barrier approximation. For Ti and Sc contacts, $\rho_t \approx 0$ because of the absence of the interfacial tunneling barrier. For other metal contacts, the calculated ρ_t lies in the typical range of $10^{-9} \Omega\text{cm}^2$ which is comparable to that of the recently reported Bi/MoS₂ contact of ultralow contact resistance²². The calculated ρ_t is listed in Supplementary Table 3 which can be readily employed for contact resistance calculation and for the analysis of device transport measurements²².

We now examine the SBHs of various metal contacts. As the semiconducting band structures of MoSi₂N₄ and WSi₂N₄, especially the CBM and VBM states, are well preserved, the electron and hole SBH can be determined from the energy differences between the CBM and the Fermi level (ϵ_F) of the metal/semiconductor heterostructure, and that between the ϵ_F and the VBM via the projected band structures and the PDOS data (see Supplementary Fig. 2). The SM plot of the metal-contacted MoSi₂N₄ and WSi₂N₄ is shown in Fig. 5b–e for both electron-type and hole-type SBH. In general, the SM plot of the electron-type SBH exhibits a positive slope with increasing metal work function. Conversely, the hole-type SBH exhibits a negative slope as

dictated by the SM relation in Eq. (2). A linear fit across the 11 metal contacts reveals a remarkably large slope parameter of $S_e \approx S_h = 0.69$ for MoSi₂N₄ where S_e and S_h denote electron and hole slope parameters, and $S_e = 0.77$ and $S_h = 0.76$ for WSi₂N₄. Although being lower than that of the 2D/2D and 3D/2D VDW-type contacts^{17,18}, these S values—achieved intrinsically without relying on VDW-type contact engineering—are still significantly higher than that of almost all previously reported 2D semiconductors^{14,15,27,36–51} [Fig. 1e], such as MoS₂ monolayer and bilayer, WS₂, InSe, black and blue phosphorene, arsenene, and silicene. Such exceptionally large S values, which spans over a large metal work function range of $\Delta W_M = 2.7$ eV (i.e., W_M ranging from 3.3 to 6.0 eV), indicates greater flexibility in designing metal/MoSi₂N₄ and metal/WSi₂N₄ heterostructure with a specific SBH as required by the specific device applications. For completeness, the interface potential difference ΔV is also calculated and is presented in the Supplementary Notes and Supplementary Fig. 6.

Close contacts of Pd/MoGe₂P₄ and Pd/WGe₂P₄

To further understand whether the above described built-in atomic layer protection is also present in other sister 2D semiconducting monolayers in the MA₂Z₄ family, such as the MoGe₂P₄ and WGe₂P₄ monolayers, we perform a close contact simulation of Pd/MoGe₂P₄ and Pd/WGe₂P₄ heterostructures. The close contact of Pd/MoGe₂P₄ and Pd/WGe₂P₄ heterostructures are simulated by matching the 2×2 MoGe₂P₄ (WGe₂P₄) with the $\sqrt{7} \times \sqrt{7}$ Pd(101) with a fixed interlayer separation of 2 Å. The lattice parameters are fixed to $a/b = 3.54$ Å for MoGe₂P₄ and $a/b = 3.55$ Å for WGe₂P₄. The lattice structures are shown in Fig. 6a, d for Pd/MoGe₂P₄ and Pd/WGe₂P₄, respectively. In the monolayer form, MoGe₂P₄ and WGe₂P₄ exhibit a band gap of 0.50 [Fig. 6b] and 0.48 eV [Fig. 6e], respectively, which are significantly smaller

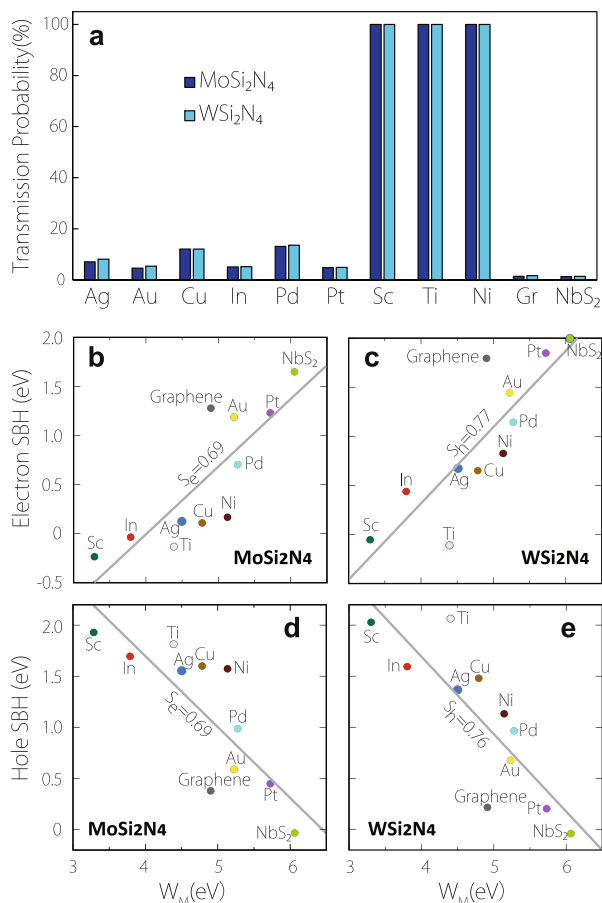


Fig. 5 \mathcal{T} and SBH of the contact heterostructures. **a** Transmission probability (\mathcal{T}) of various metal/MoSi₂N₄ and metal/WSi₂N₄ heterostructures. **b** and **c** show the Schottky–Mott plot for the electron SBH of MoSi₂N₄ and WSi₂N₄, respectively. **d** and **e** same as **b** and **c**, respectively, but for the hole SBH.

than those of the MoSi₂N₄ and WSi₂N₄ monolayer. Importantly, when forming contact heterostructures with Pd, although some metalization and mid-gap states are observed in the band structures and the projected electronic DOS calculations due to the stronger interaction between the metal atoms and the outermost P atoms Fig. 6c, f for Pd/MoGe₂P₄ and Pd/WGe₂P₄, respectively], it is remarkable to see that even with such a “close contact”, the semiconducting bands at the *K* points remain intact. The weak FLP and the protection of the semiconducting electronic bands are thus expected to present in the broader family of (Mo, W)A₂Z₄ with A = Si, Ge and Z = N, P. The physics of metal contacts to (Mo,W)Ge₂N₄ and (Mo,W)Ge₂P₄ shall form an interesting topic to explore in future works.

Metal contacts to bilayer MoSi₂N₄, MoGe₂N₄, and WGe₂N₄

We further examine three examples of metal contacts to semiconducting monolayers from the MA₂Z₄ family⁵⁸ beyond the MoSi₂N₄ and WSi₂N₄ monolayers, namely: (i) Au/bilayer–MoSi₂N₄⁵⁹; (ii) Au/MoGe₂N₄⁶⁰; and (iii) Au/WGe₂N₄ contacts. The lattice structure and the electronic band structure of Au/bilayer–MoSi₂N₄ contact are shown in Fig. 7a, b, respectively. The MoSi₂N₄/Au contact exhibits a convenient Ohmic behavior with minimal metal–semiconductor hybridization. For Au/MoGe₂N₄ [Fig. 7c–e], an Ohmic contact is also obtained while for Au/WGe₂N₄ [Fig. 7f–h], the contact type exhibits an n-type Schottky contact characteristic. Importantly, the bands correspond to the semiconducting monolayers, particularly the electronic states

around the VBM and CBM, remain well-intact in these contact heterostructures. These results thus suggest that the resistance against strong hybridization with the contacting metal appears to be a rather common feature among the septuple-layered semiconducting members of MA₂Z₄.

DISCUSSIONS

Experimentally, the *S* values are found to be lower than the theoretically calculated *S* values and such deviation is often associated with the presence of defects⁶¹. For example, the presence of *S* vacancies in metal contacts to MoS₂ has been theoretically and experimentally^{62,63} shown to create defect states that can pin the Fermi level and hence reduces the *S* value. First-principle simulations of defected metal contacts to MoSi₂N₄ and WSi₂N₄ monolayers shall quantitatively unravel how defects can affect the performance of metal contacts to these monolayers. Importantly, Sc and Ti contacts, both of which form excellent Ohmic contact with zero interfacial tunneling barrier to MoSi₂N₄ and WSi₂N₄ monolayers, are CMOS-compatible metals, thus revealing a practical contact engineering strategy for the construction of high-performance nanodevices based on MoSi₂N₄ and WSi₂N₄. For 2D metal contacts, NbS₂ can be more beneficial than graphene in terms of charge injection efficiency due to the ultralow SBH⁵⁹. Nonetheless, the identifications of 3D metal Ohmic contacts with zero SBH and zero interface tunneling barrier, such as Ti, clearly reveals the advantage of 3D metal contact over graphene and NbS₂ towards the design of high-efficiency electrical contact to MoSi₂N₄ and WSi₂N₄ monolayers.

Recently, the edge-type contact geometry has also received much research attention both^{14,61} and experimentally^{64–67}. Although the covalent-bonded heterointerface in edge-type can better facilitate charge injection, such contact geometry is faced with several challenges. The fabrication of high-quality edge-type contact remains challenging^{1,68}, and the contact resistance of edge-type contact typically lies in the range of few tens of kΩcm^{264–67}, which is one to two orders of magnitude higher than that of the face-type contact^{19,69–71} (see Supplementary Table 4). Recent work⁷² has experimentally demonstrated that the edge-type contact may not be beneficial for contact application due to the presence of pronouncing electron scatterings by defects. In addition, the edge-type contact to MoS₂ is also found to be affected by a strong FLP effect (*S* = −0.09)⁶¹. As much interfacial physics of edge-type contact has yet to be unearthed, whether appropriately designed edge contacts to the MA₂Z₄ monolayers could offer a route towards high-performance contacts remains an interesting open question to be addressed in future works. Finally, we note that the contact geometry can also take a combined edge-and face-type configuration. However, due to the large surface-to-contact ratio¹, the face-type contact is still expected to play a more dominant role in determining the physical properties of such combined-type contact.

In conclusion, we show that the septuple-layered morphology and the electronic properties of MoSi₂N₄ and WSi₂N₄ monolayers offer a mechanism, alternative and complementary to the VDW contact paradigm, for suppressing the FLP effect and for achieving efficient tunable SBH in metal contacts to MoSi₂N₄ and WSi₂N₄ monolayers. The origin of such efficient protection of the semiconducting electronic states and the suppression of the FLP is a combination of three unusual behaviors of MoSi₂N₄ and WSi₂N₄: (i) the septuple-layered structure which increases the atomic separation between the 2D semiconducting core layer and the external contacting metal atoms; (ii) the electronic structures in which the CBM and VBM states are concentrated in the inner core layer; and (iii) the relatively inert nature of the Si–N outermost layer. The DFT calculations presented here shall form a harbinger for the study of interfacial contact physics in the expansive family of MA₂Z₄. Myriads of phenomena, such as the evolution of SBH

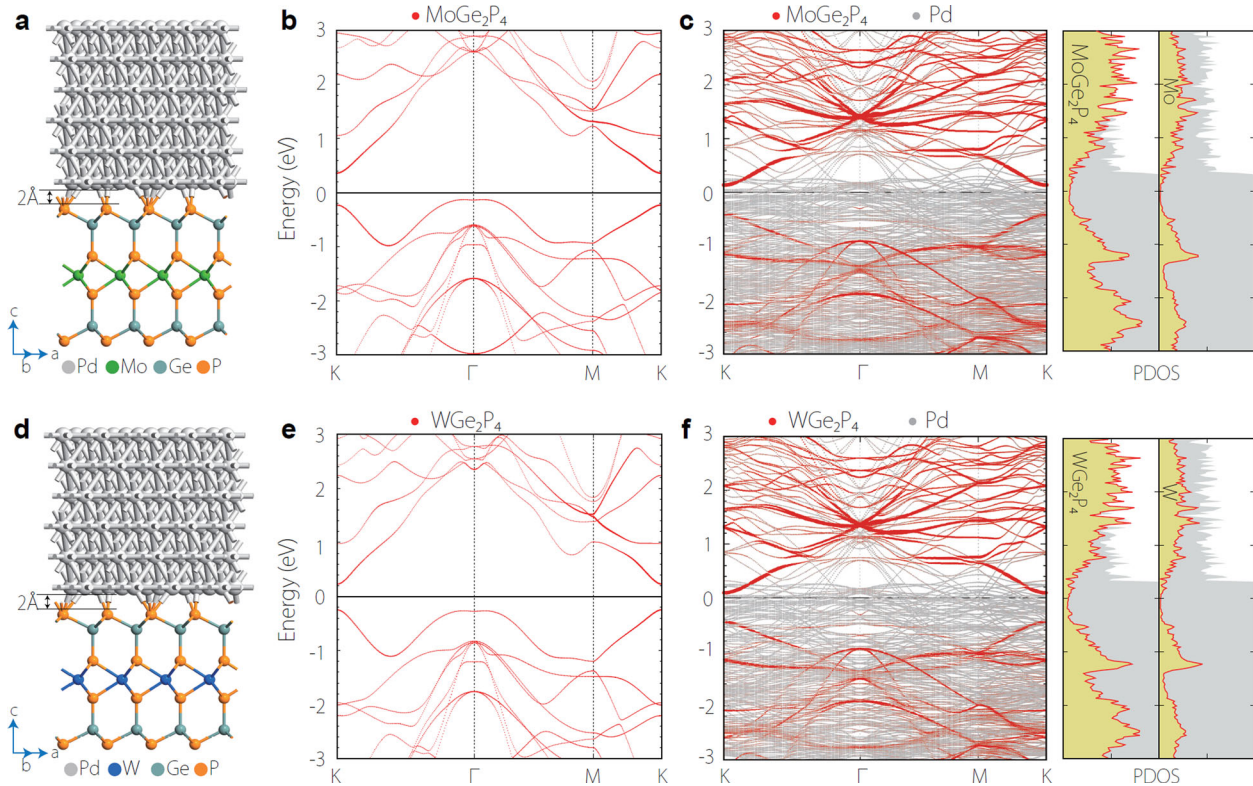


Fig. 6 Close contact simulations of Pd/MoGe₂P₄ and Pd/WGe₂P₄ with an interlayer distance of 2 Å. **a** the structure of Pd/MoGe₂P₄, **b** electronic band structure of MoGe₂P₄ monolayer, **c** the projected electronic band structure and the partial density of states of Pd/MoGe₂P₄, **d–f** same as **a–c**, respectively, for Pd/WGe₂P₄ contact.

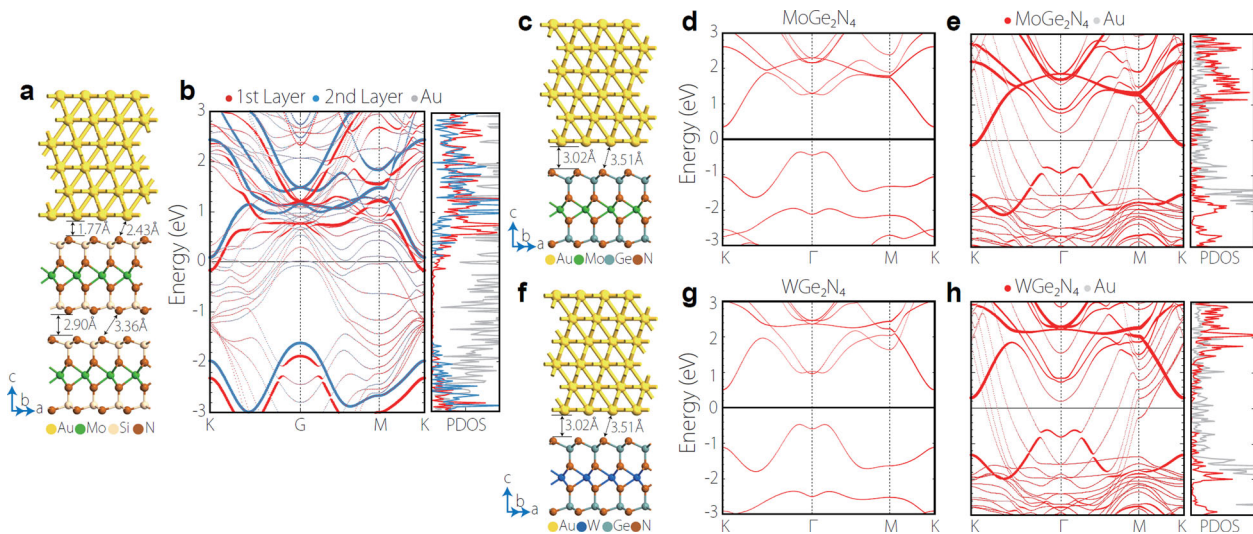


Fig. 7 Metal contacts to several other species of MA₂Z₄ monolayers. **a, b** Lattice structure, and the electronic band structure as well as the projected density of states of Au/bilayer–MoSi₂N₄ contact, respectively. **c–e** shows the lattice structure, band structure of isolated monolayer, and the band structure of the contact heterostructure with the corresponding projected density of states of Au/MoGe₂N₄ contact, respectively. **f–h** same as **c–e** but for Au/WGe₂N₄ contact.

and FLP with a different number of layers⁷³, the nature of 2D/2D and 2D/3D contacts for the other semiconducting members of the expansive MA₂Z₄ family, the design of MA₂Z₄ contact or heterostructures that can facilitate unusual non-charge transport, such as spin and valley transport⁷⁴, or neuromorphic device operations¹³, remain to be explored. As the study of MA₂Z₄ monolayer and few-layer family is still in its early infancy, the

experimental synthesis of this material class shall represent one of the most important research quests to be tackled before the physics and the device application potential of this material family can be better understood. Future computational and experimental studies of electrical contacts to MA₂Z₄ shall bring more surprises on the fundamental interface physics and chemistry, as well as the practical design of MA₂Z₄-based heterostructures and devices.

METHODS

DFT calculations

The first-principle calculations are performed using the Vienna Ab initio Simulation Package (VASP) with projector augmented wave method^{75–78}. The generalized gradient approximation (GGA) with the Perdew–Burke–Ernzerhof realization (PBE)⁷⁹ is selected for the exchange–correlation functional. A kinetic energy cut-off of 500 eV is set, and the Monkhorst–Pack k mesh⁸⁰ is used in the gamma-centered Brillouin zone with grids of $11 \times 11 \times 1$ for the geometric optimizations and electronic calculations. Atomic geometry optimizations are terminated until all forces are smaller than 10^{-3} eV/Å to ensure accuracy. The DFT-D3 Method⁸¹ with the Grimme scheme is adopted. A vacuum space of 20 Å is set in the direction perpendicular to 3D-metal/2D-semiconductor surface. The calculations for Ni contacts are spin-polarized and the initial magnetic state for Ni substrate is set as ferromagnetic.

The 3D-metal/2D-semiconductor heterostructures are simulated by six layers of metal atoms, and two bottom layers of metals are fixed in atomic optimizations to simulate the internal atoms in the electrode. The lattice matching of the heterostructures are as followed: the 1×1 MoSi₂N₄ (WSi₂N₄) matches the 1×1 Ag(111)/Au(111)/Pd(111)/Pt(111)/Ti(0001), the $\sqrt{3} \times \sqrt{3}$ MoSi₂N₄ (WSi₂N₄) matches the 2×2 Cu(111)/Ni(111)/Graphene, and the 2×2 MoSi₂N₄ (WSi₂N₄) matches the $\sqrt{3} \times \sqrt{3}$ In(101)/Sc(0001)/NbS₂. The contact faces of the metals are chosen based on those employed in previous DFT studies due to their low surface free energies and thermodynamical stability^{14,29,39}. The polycrystalline face is not considered in our calculations. To avoid the properties of MoSi₂N₄ (WSi₂N₄) being affected by mechanical stress when contacted by metals, we fixed the lattice parameters of semiconductors (MoSi₂N₄ with $a/b = 2.910$ Å, and WSi₂N₄ with $a/b = 2.913$ Å) and applied strains in the metals. The lattice mismatch for all heterostructures is less than 3.8%, and the calculation details of the metal-contacted MoSi₂N₄/WSi₂N₄ monolayers are listed in Supplementary Tables 1 and 2.

DATA AVAILABILITY

The data of this study are available from the corresponding author upon reasonable request.

CODE AVAILABILITY

The codes that are necessary to reproduce the findings of this study are available from the corresponding author upon reasonable request.

Received: 17 March 2021; Accepted: 15 July 2021;

Published online: 04 August 2021

REFERENCES

- Allain, A., Kang, J., Banerjee, K. & Kis, A. Electrical contacts to two-dimensional semiconductors. *Nat. Mater.* **14**, 1195 (2015).
- Chhowalla, M., Jena, D. & Zhang, H. Two-dimensional semiconductors for transistors. *Nat. Rev. Mater.* **1**, 16052 (2016).
- Mitta, S. B. et al. Electrical characterization of 2D materials-based field-effect transistors. *2D Mater.* **8**, 012002 (2021).
- Sze, S. M. & Ng, K. K. *Physics of Semiconductor Devices* 3rd edn (Wiley, 2006).
- Cowley, A. M. & Sze, S. M. Surface states and barrier height of metal semiconductor systems. *J. Appl. Phys.* **36**, 3212 (1965).
- Tung, R. T. Chemical bonding and Fermi level pinning at metal-semiconductor interfaces. *Phys. Rev. Lett.* **84**, 6078 (2000).
- Tung, R. T. The physics and chemistry of the Schottky barrier height. *Appl. Phys. Rev.* **1**, 011304 (2014).
- Biggs, N. et al. A roadmap for electronic grade 2D materials. *2D Mater.* **6**, 022001 (2019).
- Manzeli, S., Ovchinnikov, D., Pasquier, D., Yazyev, O. V. & Kis, A. 2D transition metal dichalcogenides. *Nat. Rev. Mater.* **2**, 17033 (2017).
- Xu, Y. et al. Contacts between two- and three-dimensional materials: ohmic, Schottky, and p-n heterojunctions. *ACS Nano* **10**, 4895 (2016).
- Fiori, G. et al. Electronics based on two-dimensional materials. *Nat. Nanotechnol.* **9**, 768 (2014).
- Liang, S., Cheng, B., Cui, X. & Miao, F. Van der Waals heterostructures for high-performance device applications: challenges and opportunities. *Adv. Mater.* **32**, 1903800 (2019).
- Wang, M. et al. Robust memristors based on layered two-dimensional materials. *Nat. Electron.* **1**, 130 (2018).
- Kang, J., Liu, W., Sarkar, D., Jena, D. & Banerjee, K. Computational study of metal contacts to monolayer transition-metal dichalcogenide semiconductors. *Phys. Rev. X* **4**, 031005 (2014).
- Gong, C., Colombo, L., Wallace, R. M. & Cho, K. The unusual mechanism of partial Fermi level pinning at metal MoS₂ interfaces. *Nano Lett.* **14**, 1714 (2014).
- Liu, Y., Huang, Y. & Duan, X. Van der Waals integration before and beyond two-dimensional materials. *Nature* **567**, 323 (2019).
- Liu, Y., Stradins, P. & Wei, S.-H. Van der Waals metal-semiconductor junction: weak Fermi level pinning enables effective tuning of Schottky barrier. *Sci. Adv.* **2**, e1600069 (2016).
- Liu, Y. et al. Approaching the Schottky-Mott limit in Van der Waals metal-semiconductor junctions. *Nature* **557**, 696 (2018).
- Wang, Y. et al. Van der Waals contacts between three-dimensional metals and two-dimensional semiconductors. *Nature* **568**, 70 (2019).
- Hong, Y.-L. et al. Chemical vapor deposition of layered two-dimensional MoSi₂ N₄ materials. *Science* **369**, 670 (2020).
- Novoselov, K. S. Discovery of 2D Van der Waals layered MoSi₂ N₄ family. *Natl. Sci. Rev.* **7**, 1842 (2020).
- Shen, P.-C. et al. Ultralow contact resistance between semimetal and monolayer semiconductors. *Nature* **593**, 211 (2021).
- Radisavljevic, B., Radenovic, A., Brivio, J., Giacometti, V. & Kis, A. Single-layer MoS₂ transistor. *Nat. Nanotechnol.* **6**, 147 (2011).
- Liu, W. et al. Role of metal contacts in designing high-performance monolayer n-type WSe₂ field effect transistors. *Nano Lett.* **13**, 1983 (2013).
- Kim, B.-K. et al. Origins of genuine ohmic Van der Waals contact between indium and MoS₂. *npj 2D Mater. Appl.* **5**, 9 (2021).
- Cao, W., Chu, J. H., Parto, K. & Banerjee, K. A mode-balanced reconfigurable logic gate built in a Van der Waals strata. *npj 2D Mater. Appl.* **5**, 20 (2021).
- Guo, Y., Liu, D. & Robertson, J. 3D behavior of Schottky barriers of 2D transition-metal dichalcogenides. *ACS Appl. Mater. Interfaces* **7**, 25709 (2015).
- Gao, J. & Gupta, M. Titanium disulfide as Schottky/ohmic contact for monolayer molybdenum disulfide. *npj 2D Mater. Appl.* **4**, 26 (2021).
- Ouyang, B., Xiong, S. & Jing, Y. Tunable phase stability and contact resistance of monolayer transition metal dichalcogenides contacts with metal. *npj 2D Mater. Appl.* **2**, 13 (2018).
- Huang, J. S., Li, P., Ren, X. X. & Guo, Z.-X. Promising properties of sub-5 nm monolayer MoSi₂ N₄ transistor. Preprint at <https://arxiv.org/abs/2105.12512> (2021).
- Cao, L., Zhou, G., Ang, L. K. & Ang, Y. S. Two-dimensional Van der Waals electrical contact to monolayer MoSi₂ N₄. *Appl. Phys. Lett.* **118**, 013106 (2021).
- Zhong, H., Xiong, W., Lv, P., Yu, J. & Yuan, S. Strain-induced semiconductor to metal transition in MA₂ Z₄ bilayers. *Phys. Rev. B* **103**, 085124 (2021).
- Kang, L. & Lin, Z. Second harmonic generation of MoSi₂ N₄ layer. *Phys. Rev. B* **103**, 195404 (2021).
- Bafekry, A. et al. MoSi₂ N₄ single-layer: a novel two-dimensional material with outstanding mechanical, thermal, electronic, optical, and photocatalytic properties. *J. Phys. D: Appl. Phys.* **54**, 155303 (2021).
- Li, S. et al. Valley-dependent properties of monolayer MoSi₂ N₄, WSi₂ N₄ and MoSi₂ As₄. *Phys. Rev. B* **102**, 235435 (2020).
- Guo, Y. & Robertson, J. Band structure, band offsets, substitutional doping, and Schottky barriers of bulk and monolayer InSe. *Phys. Rev. Mater.* **1**, 044004 (2017).
- Shen, T., Ren, J.-C., Liu, X., Li, S. & Liu, W. Van der Waals stacking induced transition from Schottky to Ohmic contacts: 2D metals on multilayer InSe. *J. Am. Chem. Soc.* **141**, 3110 (2019).
- Gao, N., Zhou, S., Liu, N., Bai, Y. & Zhao, J. Selecting electrode materials for monolayer ReS₂ with an Ohmic contact. *J. Mater. Chem. C* **6**, 6764 (2018).
- Tang, H. et al. Schottky contact in monolayer WS₂ field effect transistors. *Adv. Theory Simul.* **2**, 1900001 (2019).
- Wang, Y. et al. Does p-type ohmic contact exist in WSe₂ metal interfaces? *Nanoscale* **8**, 1179 (2016).
- Zhong, H. et al. Interfacial properties of monolayer and bilayer MoS₂ contacts with metals: beyond the energy band calculations. *Sci. Rep.* **6**, 21786 (2016).
- Pan, Y. et al. Monolayer phosphorene-metal contacts. *Chem. Mater.* **28**, 2100 (2016).
- Pan, Y. et al. Schottky barriers in bilayer phosphorene transistors. *ACS Appl. Mater. Interfaces* **9**, 12694 (2017).
- Zhang, X. et al. Three-layer phosphorene-metal interfaces. *Nano Res.* **11**, 707 (2018).
- Li, J. et al. Electrical contacts in monolayer blue phosphorene devices. *Nano Res.* **11**, 1834 (2018).
- Zhang, H. et al. Interfacial properties of monolayer antimonene devices. *Phys. Rev. Appl.* **11**, 064001 (2019).
- Yan, J. et al. Monolayer tellurene/metal contacts. *J. Mater. Chem. C* **6**, 6153 (2018).

48. Liu, Y. et al. Approaching the Schottky-Mott limit in Van der Waals metal-semiconductor junctions. *Nature* **557**, 696 (2018).
49. Das, S., Chen, H.-Y., Penumatcha, A. V. & Appenzeller, J. High performance multilayer MoS₂ transistors with Scandium contacts. *Nano Lett.* **13**, 100 (2013).
50. Lv, C. et al. Electrical contact barriers between a three-dimensional metal and layered SnS₂. *ACS Appl. Mater. Interfaces* **12**, 15830 (2020).
51. Yoon, H. H. et al. Negative Fermi level pinning effect of metal/n-GaAs(001) junction induced by a graphene interlayer. *ACS Appl. Mater. Interfaces* **11**, 47182 (2019).
52. Popov, I., Seifert, G. & Tomanek, D. Designing electrical contacts to MoS₂ monolayers: a computational study. *Phys. Rev. Lett.* **108**, 156802 (2012).
53. Kong, L. et al. Doping-free complementary WSe₂ circuit via Van der Waals metal integration. *Nat. Commun.* **11**, 1866 (2020).
54. Kim, G.-S. et al. Schottky barrier height engineering for electrical contacts of multilayered MoS₂ transistors with reduction of metal-induced gap states. *ACS Nano* **12**, 6292 (2018).
55. Farmanbar, M. & Brocks, G. First-principles study of Van der Waals interactions and lattice mismatch at MoS₂/metal interfaces. *Phys. Rev. B* **93**, 085304 (2016).
56. Bokdam, M., Brocks, G. & Kelly, P. J. Large potential steps at weakly interacting metal-insulator interfaces. *Phys. Rev. B* **90**, 201411 (2014).
57. Simmons, J. G. Generalized formula for the electric tunnel effect between similar electrodes separated by a thin insulating film. *J. Appl. Phys.* **34**, 1793 (1963).
58. Wang, L. et al. Intercalated architecture of MA₂Z₄ family layered Van der Waals materials with emerging topological, magnetic and superconducting properties. *Nat. Commun.* **12**, 2361 (2021).
59. Wu, Q., Cao, L., Ang, Y. S. & Ang, L. K. Semiconductor-to-metal transition in bilayer MoSi₂N₄ and WSi₂N₄ with strain and electric field. *Appl. Phys. Lett.* **118**, 113102 (2021).
60. Nguen, C., Hoang, N. V., Phuc, H. V., Sin, A. Y. & Nguyen, C. V. Two-dimensional boron phosphide/MoGW₂N₄ Van der Waals heterostructure: a promising tunable optoelectronic material. *J. Phys. Chem. Lett.* **12**, 5076 (2021).
61. Fang, Q. et al. Junction-configuration-dependent interfacial electronic states of a monolayer MoS₂/metal contact. *J. Mater. Chem. C* **7**, 3607 (2019).
62. Kim, C. et al. Fermi level pinning at electrical metal contacts of monolayer molybdenum dichalcogenides. *ACS Nano* **11**, 1588 (2017).
63. Bussolotti, F., Yang, J., Kawai, H., Wong, C. P. Y. & Goh, K. E. J. Impact of S-Vacancies on the charge injection barrier at the electrical contact with the MoS₂ monolayer. *ACS Nano* **115**, 2686 (2021).
64. Guimaraes, M. H. D. et al. Atomically thin ohmic edge contacts between two-dimensional materials. *ACS Nano* **10**, 6392 (2016).
65. Jain, A. et al. One-dimensional edge contacts to a monolayer semiconductor. *Nano Lett.* **19**, 6914 (2019).
66. Choi, H. et al. Edge contact for carrier injection and transport in MoS₂ field-effect transistors. *ACS Nano* **13**, 13169 (2019).
67. Cheng, Z. et al. Immunity to contact scaling in MoS₂ transistors using in situ edge contacts. *Nano Lett.* **19**, 5077 (2019).
68. Zheng, Y., Gao, J., Han, C. & Chen, W. Ohmic contact engineering for two-dimensional materials. *Cell Rep. Phys. Sci.* **2**, 100298 (2021).
69. Cui, X. et al. Low-temperature ohmic contact to monolayer MoS₂ by Van der Waals bonded Co/h-BN electrodes. *Nano Lett.* **17**, 4781 (2017).
70. Cui, X. et al. Multi-terminal transport measurements of MoS₂ using a Van der Waals heterostructure device platform. *Nat. Nanotechnol.* **10**, 534 (2015).
71. Leong, W. S. et al. Low resistance metal contacts to MoS₂ devices with nickel-etched-graphene electrodes. *ACS Nano* **9**, 869 (2015).
72. Wong, L.-W. et al. Site-specific electrical contacts with the two-dimensional materials. *Nat. Commun.* **11**, 3982 (2020).
73. Wang, Q., Shao, Y., Gong, P. & Shi, X. Metal 2D multilayered semiconductor junctions: layer-number dependent Fermi level pinning. *J. Mater. Chem. C* **8**, 3113 (2020).
74. Chen, J.-R. et al. Control of Schottky barriers in single layer MoS₂ transistors with ferromagnetic contacts. *Nano Lett.* **13**, 3106 (2013).
75. Kresse, G. & Hafner, J. Ab Initio molecular dynamics for liquid metals. *Phys. Rev. B* **47**, 558 (1993).
76. Kresse, G. & Furthmuller, J. Efficiency of Ab-Initio total energy calculations for metals and semiconductors using a plane-wave basis set. *Comput. Mater. Sci.* **6**, 15 (1996).
77. Blöchl, P. E. Projector augmented-wave method. *Phys. Rev. B* **50**, 17953 (1994).
78. Kresse, G. & Joubert, D. From ultrasoft pseudopotentials to the projector augmented-wave method. *Phys. Rev. B* **59**, 1758 (1999).
79. Perdew, J. P., Burke, K. & Ernzerhof, M. Generalized gradient approximation made simple. *Phys. Rev. Lett.* **77**, 3865 (1996).
80. Monkhorst, H. J. & Pack, J. D. Special points for Brillouin-zone integrations. *Phys. Rev. B* **13**, 5188 (1976).
81. Grimme, S., Antony, J., Ehrlich, S. & Krieg, H. A consistent and accurate Ab Initio parametrization of density functional dispersion correction (DFT-D) for the 94 elements H-Pu. *J. Chem. Phys.* **132**, 154104 (2010).

ACKNOWLEDGEMENTS

This work is supported by SUTD Start-Up Grant (SRG SCI 2021 163), Singapore Ministry of Education (MOE) Tier 2 Grant (No. 2018-T2-1-007), and SUTD-ZJU IDEA Visiting Professor Grant (SUTD-ZJU (VP) 202001). Q.W. is supported by SUTD Ph.D. Fellowship. S.A.Y. acknowledges the support of Singapore MOE AcRF Tier 2 (Grant No. MOE2017-T2-2-108). C.H.L. is supported by the Singapore Ministry of Education Academic Research Fund Tier I (WBS No. R-144-000-435-133). All the calculations were carried out using the computational resources provided by the National Supercomputing Centre (NSCC) Singapore.

AUTHOR CONTRIBUTIONS

Y.S.A. and L.C. conceptualized and initiated this project. Q.W. performed the first principle simulation and analysis. W.W. and G.W. supported the simulation. L.K.A. and S.A.Y. took on advisory roles and co-supervised the project. Y.S.A. wrote most of the manuscript and all authors reviewed the manuscript. The manuscript reflects the contributions of all authors.

COMPETING INTERESTS

The authors declare no competing interests.

ADDITIONAL INFORMATION

Supplementary information The online version contains supplementary material available at <https://doi.org/10.1038/s41699-021-00251-y>.

Correspondence and requests for materials should be addressed to L.C., L.K.A., S.A.Y. or Y.S.A.

Reprints and permission information is available at <http://www.nature.com/reprints>

Publisher's note Springer Nature remains neutral with regard to jurisdictional claims in published maps and institutional affiliations.



Open Access This article is licensed under a Creative Commons Attribution 4.0 International License, which permits use, sharing, adaptation, distribution and reproduction in any medium or format, as long as you give appropriate credit to the original author(s) and the source, provide a link to the Creative Commons license, and indicate if changes were made. The images or other third party material in this article are included in the article's Creative Commons license, unless indicated otherwise in a credit line to the material. If material is not included in the article's Creative Commons license and your intended use is not permitted by statutory regulation or exceeds the permitted use, you will need to obtain permission directly from the copyright holder. To view a copy of this license, visit <http://creativecommons.org/licenses/by/4.0/>.

© The Author(s) 2021